Radiometric spectral fusion of VNIR and SWIR hyperspectral cameras

Federico Grillini*, Jean-Baptiste Thomas and Sony George
The Norwegian Colour and Visual Computing Laboratory, IDI-NTNU, Gjøvik, Norway
**** corresponding author: federico.grillini@ntnu.no***

Abstract

When two hyperspectral cameras are sensitive to complementary portions of the electromagnetic spectrum it is fundamental that the calibration processes conducted independently lead to comparable radiance values, especially if the cameras show a shared spectral interval. However, in practice, a perfect matching is hard to obtain, and radiance values that are expected to be similar might differ significantly. In the present study we propose to introduce an ulterior linear correcting factor in the radiometric calibration pipeline of two hyperspectral cameras, operating in the visible near infrared (VNIR) and short wave infrared (SWIR) intervals. The linearity properties of both cameras are preliminarily assessed, conducting acquisitions on five standardized targets, and highlighting noise at the sensors level and different illumination fields as the main causes of radiance mismatch. The correction step that we propose allows the retrieval of accurate and smoothly connected VNIR-SWIR reflectance factor curves.

Introduction

The ability to retrieve more than colour information from images is highly regarded amongst scientists whose goal is to effectively study the material features of objects in a non-invasive manner, such as in the fields of cultural heritage [1], medical [2], and quality control [3]. Imaging techniques carry a great advantage over their punctual analytical counterparts, since they can capture information along the spatial dimensions, allowing the efficient *mapping* of the feature under examination [4].

One of the most popular imaging technique exploited for material mapping is Imaging Spectroscopy. Originally exploited by NASA to analyze satellite images [5], it found numerous applications, first limited to the domain of airborne remote sensing [6], then in laboratory use, for proximal sensing applications [7]. Imaging Spectroscopy allows the pixel-wise observation of the spectral information contained in a scene. Multispectral (MS) and Hyperspectral (HS) systems are differentiated according to the number of bands and the bandwidth of their sensors [8], thus, for the same spectral interval, a HS camera will produce an image sampled at a higher spectral resolution.

The materials usually adopted to build the sensors possess a limited range of sensitivity to light across the electromagnetic spectrum. For this reason, it is not currently possible to build a sensor that is able to capture simultaneously all of the electromagnetic field energy. Different ranges can however be acquired using sensors constructed with different materials. This is the case for the visible near infrared (VNIR) and short wave infrared (SWIR) regions, for which at least two sensors are necessary to capture the whole range. The former spans from the visible region of the electromagnetic spectrum $(400-700)$ nm to the IR-A $(700-1400)$ nm, whilst the latter encloses the IR-B, from 1400 nm to 3000 nm.

For most laboratory applications of HS imaging, the end goal is to analyze the reflectance properties of the acquired materials. In order to achieve this physical quantity, the raw signal recorded by the cameras must be first transformed into Radiance (L) via radiometric calibration, eliminating the influence of the camera and acquisition parameters [9]. At this stage, the signal carries information regarding the illumination and the observed material. If the two cameras under study share an overlapping region in their spectral ranges, then the radiances in the overlap region must match. Without a radiance match, it will not be possible to retrieve a continuous and smooth reflectance factor curve of the objects under study. For a variety of applications, a smooth and continuous reflectance factor curve is not only a sign of optimal joint calibration, but a powerful asset as well, as it could facilitate operations of spectral matching, which are often used in pigment mapping for example [10]. Contrarily to the expectations, we will show how in our setup there exists a mismatch between the VNIR and SWIR radiance curves in the shared spectral interval, between 950 nm and 1000 nm.

The simultaneous use of HS cameras sensitive to different spectral intervals has been extensively studied in airborne applications [11]. In a typical framework, the two cameras are placed side by side on the aircraft and acquire the scene at the same time. In post processing, the two images having different spatial and spectral resolutions are co-registered and fused in order to form a unique output. Pansharpening [12] and its fully-spectral extension hypersharpening [13] techniques have been developed to overcome the issue of fusing images coming from different devices. Hardware solutions were developed as well, headlined by co-boresighted systems, that however reaped little success, due mainly to high costs and fragility [14].

In hypersharpening, the issue of spectral mismatch in overlapping regions is generally not treated. The quality evaluation of the final fused spectral image usually relies on a fictional ground truth, derived from the usage of Wald's protocol [15]. The ground truth is then composed based on the available dataset, which might already suffer from a radiance mismatch, if the systems adopted share a spectral working interval. Moreover, depending on the sharpening technique selected, one can prioritize the preservation of spatial information over spectral information, and vice versa. The overlapping bands of systems are also prone to the presence of noise, and are generally discarded in those applications, accepting *spectral holes* in the final images.

The work that we present here is a first step of investigations that will eventually lead to the effective combination of VNIR and SWIR HS images, similarly to a hypersharpening framework. The first *chapter* of this larger study concerns the spectral matching of two cameras in a proximal sensing application. Therefore, the spatial information provided by the cameras is momentarily set aside, and used to average regions of interest in the image, in order to reduce the influence of individual

fluctuations in the collected spectra.

We propose to match the VNIR and SWIR radiance curves by introducing a linear corrective factor in the calibration workflow. For that we assume a linear behavior of both cameras with respect to changes in radiance intensities and camera parameters such as integration time.. The contributions of this study are the verification of the linear behavior of both HS cameras, and the proposition of a preliminary framework for spectral matching.

Material and Methods

Experimental setup

In this work, the dual acquisition system comprises two HS cameras: HySpex VNIR1800 and HySpex SWIR384, manufactured by Norsk Elektrikk Optikk (NEO). Both systems exploit the push-broom technology, in which at each acquisition, a spatial line is acquired in its entire spectrum. In this setup, the cameras and the illumination are kept in fixed positions, whilst a trolley shifts the scene across the field of view of the capturing system. Being line-scanners, both cameras allow incoming light from a narrow slit and then onto a diffraction grating which scatters the different wavelengths before they are captured by the photosensitive material and transduced in electronic signals.

In a simultaneous acquisition, the translational stage moves at a speed synchronized with the integration times and frame periods of both cameras. In the dual camera setup, the selection of the relative frame periods is critical to obtain images that are neither saturated nor under exposed.

The VNIR camera exploits a CMOS sensor sensitive in the interval from 400 nm to 1000 nm, sampling channels at a spectral resolution of 3.26 nm, which results in producing 186 spectral bands. The SWIR camera, which sensor is made of MCT (Mercury-Cadmium-Telluride), is sensible to light from 950 nm to 2500 nm, sampling every 5.45 nm, and outputting 288 spectral bands. The overlapping area between the VNIR and SWIR range is found from 950 nm to 1000 nm, and it includes 15 VNIR bands and 9 SWIR bands.

The two cameras differ greatly in spatial resolution: although having similar fields of view (17° and 16°, respectively), the VNIR camera acquires 1800 pixel per line, whereas the SWIR camera only 384. Thus, the spatial resolutions are roughly in a ratio 5 : 1, with the pixels sizes being $50\,\mu m$ and $220\,\mu m$, respectively, at an acquisition distance of 30 cm.

The targets used for this experiment are two different Spectralon targets: a 4-step-Spectralon $[99\%, 50\%, 25\%, 12.5\%]$ and a Standard gray target (G). The reflectances of the 5 standardized samples are provided by the manufacturers and defined in the interval between 250 nm and 2500 nm at steps of 1 nm.

The illumination system deployed two halogen lights placed next to the cameras. Since the cameras are arranged side by side, only the closer light forms a 45° angle with the correspondent camera. The experimental setup is schematically represented in Fig. 1.

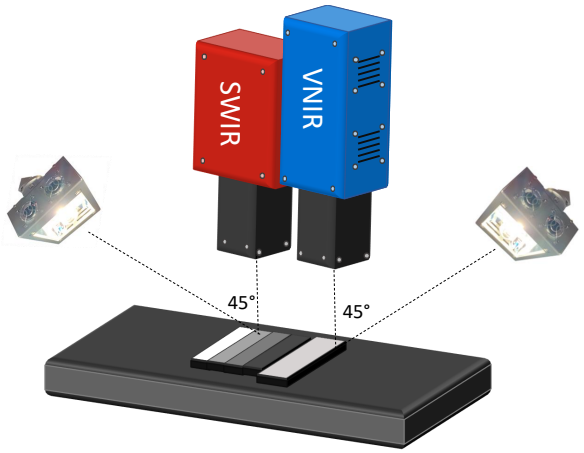

Figure 1. *Experimental setup. The standardized targets are placed at* 30 *cm from the cameras and illuminated by halogen lights at* 45°*. The trolley moves at a speed that is synchronized with the integration times of the cameras.*

Radiometric Correction

The digital numbers reported as pixel values in the RAW image are influenced by the type of deployed sensor, and by the effects of the selected acquisition parameters. To move into a camera-independent space that aims to represent unambiguously the observed scene it is necessary to get rid of such influence. With radiometric correction [9], the scene radiance is reverse engineered, exploiting the previous knowledge that we have about camera calibration and settings. The correction to obtain the radiance image $\mathbf{L}$ can be summed up with the following equation:

$$\mathbf{L}(\mathbf{x},\lambda) = \frac{[\mathbf{RAW}(\mathbf{x},\lambda) - \mathbf{BG}(\mathbf{x},\lambda)] \cdot h \cdot c}{QE(\lambda) \cdot \mathbf{RE}(\mathbf{x},\lambda) \cdot SF \cdot A \cdot t \cdot \omega \cdot \Delta\lambda(\lambda) \cdot \lambda} \quad (1)$$

in which x defines the pixel index, **RAW** is the image signal expressed in digital counts, **BG** is the background (dark current) image acquired averaging 200 lines with the same acquisition parameters and closed shutter, $h \cdot c$ is the Planck's constant times speed of light expressed in $[J \cdot m]$. QE represents the quantum efficiency of the sensor, whilst **RE** is the gain matrix, a calibration-derived matrix with unitary mean obtained by capturing an integrating sphere. The scaling factor SF represents the digital numbers per photoelectron and is associated to the camera under consideration. The integration time, camera aperture and pixel field of view are reported with t, A, and ω, and expressed in units of $[s]$, $[m^2]$, and $[sr]$, respectively. The terms $\Delta\lambda$ and λ represent the bandwidths (Full Width at Half Maximum) and central wavelength of the spectral channels, respectively. The units of radiance are $[W \cdot sr^{-1} \cdot m^{-2} \cdot nm^{-1}]$. All of the aforementioned quantities are accessible from the header file that accompanies each acquisition output.

Flat-field correction is performed by normalizing the whole spectral image with a spectral line derived from the acquisition of a uniform target (**FF**). With this procedure, it is possible to correct the non-uniform illumination field that may arise from the experimental setup. We can thus substitute the term $[\mathbf{RAW}(\mathbf{x},\lambda) - \mathbf{BG}(\mathbf{x},\lambda)]$ in Eq. 1 with:

$$\mathbf{RAW}^*(\mathbf{x},\lambda) = \frac{\mathbf{RAW}(\mathbf{x},\lambda) - \mathbf{BG}(\mathbf{x},\lambda)}{\mathbf{FF}(\mathbf{x},\lambda) - \mathbf{BG}(\mathbf{x},\lambda)} \quad (2)$$

Eq. 1 is applied on the RAW images of the two cameras independently. At this stage, it is expected that the radiances coming from VNIR and SWIR in the overlapping area (950 nm to 1000 nm) are matching, or close to match. However, this is not the case, as it is possible to observe in Fig. 2.

Linearity Evaluation

To study the linear behavior of the cameras we propose two approaches, depending on the considered signal. Raw digital

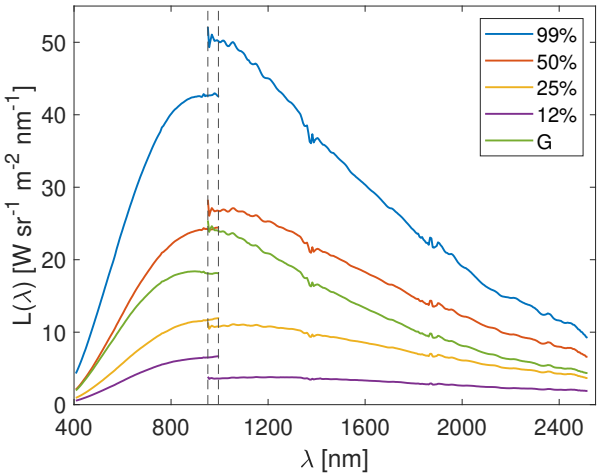

Figure 2. *Radiance plot at fixed integration times (50 ms for VNIR, 15 for SWIR) of the 5 standardized targets. The VNIR/SWIR mismatch is observable with different magnitudes in all instances.*

counts linearity can be evaluated by observing the responses of the cameras when varying the observed reflective tiles and the integration times of the acquisitions, whereas radiance linearity can only be evaluated in the first instance, since the influence of integration time is annihilated by radiometric correction. Other degrees of freedom could be added by applying a neutral density (ND) filter or by changing the intensity of the light sources, but those ways were not explored in this preliminary work.

During the acquisition campaign, 6 different integration times are selected for each camera in the simultaneous capture. The VNIR integration times were set to $[60, 50, 40, 30, 20, 10]$ ms, whereas the SWIR times were set to $[18, 15, 12, 9, 6, 3]$ ms.

Masks are manually cropped from the VNIR image and transformed into SWIR coordinates, in order to ensure the selection of the same spatial areas between the two acquisition modalities. RAW values are extracted from the masks and converted into radiance by using Eq. 1. Then, the corresponding radiance spectra are obtained by averaging along the spatial dimensions.

The linear behavior is assessed spectrally: for each band, the values corresponding to the 5 standardized tiles or to the 6 integration times are extracted. A linear model is fitted via regression, while its parameters are stored for evaluation. The slope of the fitted line can give insights on the influence of the selected variable (reflective intensity or integration time), whereas the coefficient of determination of the model R^2 can be exploited as linearity indicator:

$$R^2 = 1 - \frac{\sum_{i=1}^{N} (y_i - \hat{y}_i)^2}{\sum_{i=1}^{N} (y_i - \bar{y})^2} \tag{3}$$

In Eq. 3, y represents the observed signal, $\hat{y}$ its estimation, $\bar{y}$ the mean of the observations, and N the total number of samples. The coefficient of determination R^2 is defined in the interval $[-1, 1]$, with 1 indicating a perfectly linear model.

Matching correction

Once the linear behaviors of both cameras are assessed, we can proceed to introduce a multiplicative correcting factor in the radiometric correction pipeline, to match the VNIR and SWIR radiances in the overlapping spectral interval. Instead of matching the SWIR curves to the VNIR curves or vice versa, both ranges are corrected. As observed in Fig. 2, the SWIR curves are dispersed, while it is known that the VNIR camera suffers from a low signal-to-noise ratio (SNR) at higher wavelengths (Fig. 3) [16].

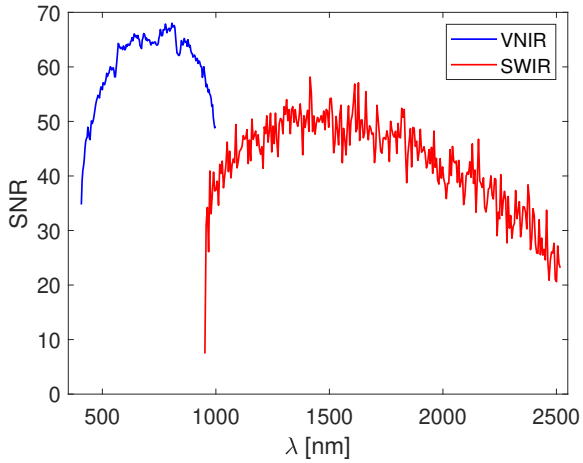

Figure 3. *Signal-to-Noise Ratio by wavelength for the two HS cameras. The computation is performed on the 99% reflective tile at the highest integration time (60 ms for VNIR and 18 ms for SWIR). For each band, the SNR is obtained as the ratio between the mean value and the standard deviation: $SNR(\lambda) = \mu/\sigma$*

Since there are infinite possibilities for the two curves to match by applying correcting factors, we decided to design an optimization process that aims to minimize the reconstruction error on the retrieved reflectances.

For a single acquisition at a specific integration time, the output of the optimization is formed by two vectors, $\mathbf{\Phi}$ and $\mathbf{\Psi}$, each constituted of 5 elements (as many as the considered reflective tiles) such that $\mathbf{\Phi} = (\phi_w, \phi_2, \phi_3, \phi_4, \phi_5)^T$ and $\mathbf{\Psi} = (\psi_w, \psi_2, \psi_3, \psi_4, \psi_5)^T$ for VNIR and SWIR respectively, and corresponding in order to the tiles: 99%, 50%, 25%, 12.5%, and G. During the reflectance retrieval operation, the white tile with average reflectance of 99% is selected as reference, and in the notation can be recognized by the subscript w. The necessary condition for the matching of VNIR and SWIR curves is that $\frac{\mathbf{\Phi}}{\mathbf{\Psi}} = \frac{O^s}{O^v}$, in which O^v and O^s are subsets of the radiance curves in the overlap region, for VNIR (v) and SWIR (s) respectively. These two vectors have length $q = 9$, i.e. the number of SWIR bands in the interval. Since the two curves are sampled at different frequencies, a linear interpolation was performed to down-sample the VNIR curve to match the spectral resolution and central wavelengths of SWIR to reduce the risk of interpolating error that may arise from an up-sampling step. The optimization problem to be solved can be formulated as:

$$\underset{\mathbf{\Phi},\mathbf{\Psi}}{argmin} \left[\sum_{i=1}^{N} \left(\rho_i^v - \frac{L_i^v \cdot \mathbf{\Phi}}{L_i^{wv} \cdot \phi_w} \rho_i^{vw} \right)^2 + \sum_{j=1}^{M} \left(\rho_j^s - \frac{L_j^s \cdot \mathbf{\Psi}}{L_j^{ws} \cdot \psi_w} \rho_j^{sw} \right)^2 \right]$$
$$s.t. \; \frac{\mathbf{\Phi}}{\mathbf{\Psi}} = \frac{O^s}{O^v} = \frac{L^s_{(950-1000nm)}}{L^v_{(950-1000nm)}} \tag{4}$$

in which the symbol w indicates the white tile used as reference. N and M are the number of VNIR and SWIR bands, respectively, while ρ is the known reflectance target of the standardized tiles. The sum of squared errors of VNIR and SWIR is used as function to be minimized. The optimization is run in Matlab using the optimization toolbox [17]:

```
%define optimization as a minimization
    problem
prob = optimproblem('ObjectiveSense','min');
%initialize the dimensions of correcting
    factors
x = optimvar('x',2,5);
%equality constraint as in Eq.4
EqCon = x(1,:)./x(2,:) == mean(Os./Ov);
prob.Constraints.EqCon = EqCon;
%initialize the correcting factor to no
    correction
start.x = ones(2,5);
%define the cost function
prob.Objective = sum((Lv.*start.x(1,:)./
    (Lvw*start.x(1,1)).*rho_v - rho_v)^2) +
    sum((Ls.*start.x(2,:)./
    (Lsw*start.x(2,1)).*rho_s - rho_s)^2)
%solution commands
sol = solve(prob,start);
correcting_factors = sol.x;
```

Listing 1. *Sample Matlab code for optimization*

The correcting factors contained in $\mathbf{\Phi}$ and $\mathbf{\Psi}$ are then applied in a multiplicative way to the radiance spectra of VNIR and SWIR, respectively. In this preliminary work and with this reduced sample size, the factors are applied to the same objects used for calibration. However, the general idea is to apply the corrective factor to the rest of the spectral images as well.

Results

Linearity evaluation

To verify the linear behavior of the HS cameras, we acquired 5 standardized tiles at 6 integration times. To analyze the results, we propose to consider the observations in both RAW mode and radiance mode, while we differentiate between linearity by integration time and linearity by reflectance. For the different instances we will use the following notation: **(a)** for RAW with fixed reflective tiles, **(b)** for radiance with fixed tiles, **(c)** for RAW with fixed integration times, and **(d)** for radiance with fixed integration times. For each instance and at every wavelength, we fit a linear model and retrieve its slope and coefficient of determination R^2.

Fig. 4 reports the values of the normalized slopes by wavelength in each of the aforementioned instances. We can notice that the values are generally positive, except for **(b)**, in which the scale changes as well. Indeed, the influence of the integration time is expected to be null on radiance signals, and such slope values indicate rather flat and noisy curves. The slopes generally follow closely the shape of the considered spectra in case of RAW mode, whilst for radiance mode with fixed integration times **(d)**, the curves all collapse in the same locus, meaning that the camera responses behave similarly for all tiles when the integration time is varied.

Similarly, Fig. 5 reports the coefficients of determination R^2 along the wavelengths for both cameras. This measure is used as linearity indicator.

When the tiles are varied, in instances **(c)** and **(d)**, the values of R^2 approach 1, implying a very high degree of linearity. The case of **(b)** can confirm the observation made with the slope examination, and linearity is not achieved due to the fact that the integration time has been accounted for during radiometric correction. The most interesting case is reported in **(a)**. Here, a high degree of linearity is achieved in the VNIR range, while a rather varying outcome is present for SWIR. When darker tiles are analyzed, we can observe how the values of R^2 are much lower at shorter wavelengths. This result might be due to the presence of noise in the sensor, which leads to distorted values, when both the

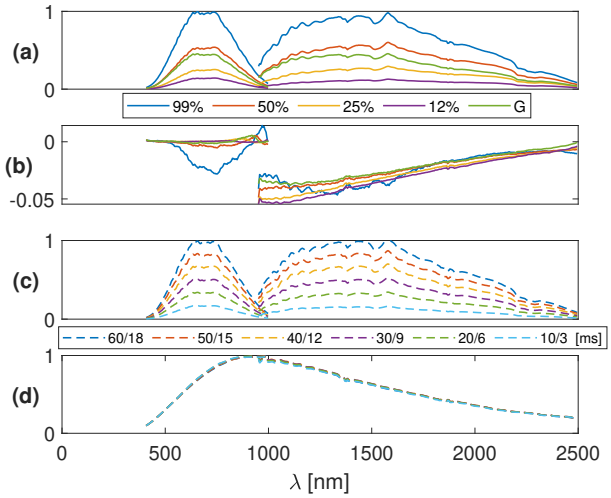

Figure 4. *Slopes by wavelengths computed from the fitting of linear models.* ***(a):*** *RAW data, fixed tiles.* ***(b):*** *radiance data, fixed tiles.* ***(c):*** *RAW data, fixed integration times.* ***(d):*** *radiance data, fixed integration times.*

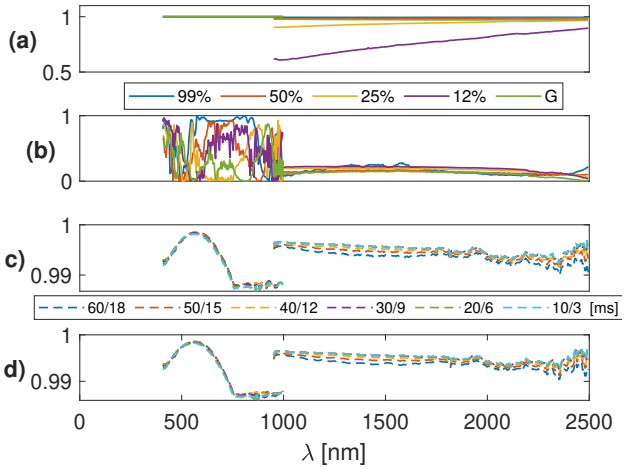

Figure 5. *Coefficient of determination R^2 by wavelengths computed from the fitting of linear models.* ***(a):*** *RAW data, fixed tiles.* ***(b):*** *radiance data, fixed tiles.* ***(c):*** *RAW data, fixed integration times.* ***(d):*** *radiance data, fixed integration times.*

integration time and the average reflectance of the target are decreased. Indeed, if we consider the histogram of intensities of the recorded signals against background noise (Fig. 6), we observe a progressive overlap as we approach the described instances. The background image is obtained prior to the acquisition by averaging 200 frames with the camera settings of the acquisition and closed shutter.

The largest presence of noise in the SWIR spectral interval is found at shorter wavelengths, in the region in which the overlap with VNIR occurs. Noise leads to differing radiance curves, which eventually leads to non-matching radiance and reflectance values between VNIR and SWIR.

We can conclude that the two examined HS cameras generally possess linear behaviors, confirming the expectations. As introduced in [18], there exists a range of integration times for which this statement is true, as we observe the failing of linearity for the SWIR camera when the exposure values decrease. The verification of the linearity of both VNIR and SWIR cameras justify at this point the introduction of linear correcting factors in the radiometric correction pipeline.

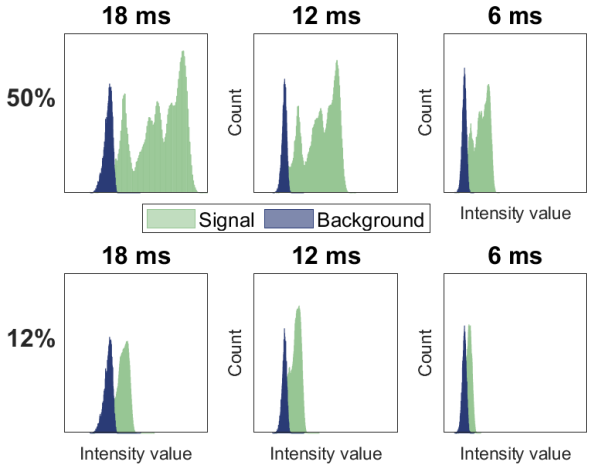

Figure 6. *Recorded signal against background signal (dark current) for the SWIR camera. As we shift towards darker reflective targets (12%) and lower integration times, the overlap between the two signals becomes larger, indicating more unstable results. For readability, the values on the axes have been omitted. The Intensity value axis ranges from 0 to 48000 digital counts, whereas the Count axis ranges from 0 to 15000.*

VNIR-SWIR Matching

The effects of the optimization process adopted to match the radiances and consequently the reflectances of the VNIR and SWIR curves are analyzed in terms of spectral similarity between the retrieved reflectances and those provided by the manufacturer of the reference tiles. The Mean Square Error (MSE) is computed for the VNIR range, the SWIR range, and for both ranges combined. Fig. 7 reports the three instances, comparing the reflectances obtained via standard procedure, via the described optimization, and via matching of the SWIR curves to VNIR (without optimization). In the last instance, the ratio between the spectra in the overlapping interval is used to correct the SWIR radiance.

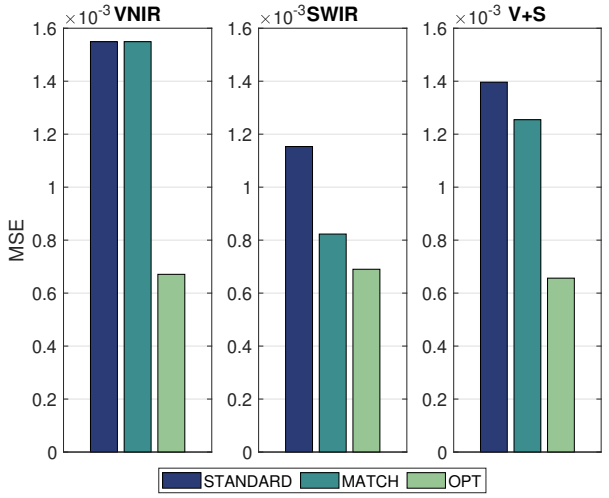

Figure 7. *Reconstruction error of reflectances expressed in terms of MSE. The spectra proposed by the optimization process follow more closely those provided by the manufacturers. The direct matching can provide better results than the standard procedure, but it matches the SWIR curves to the VNIR ones, assuming that the VNIR radiances are correct. The bars are computed excluding the reconstructions on the 99% reflective tile, since it was used as reference and thus, always perfectly reconstructed.*

To better understand the impact of the correction performed on the radiance curves, Fig. 8 reports heat maps in which the values represent the percentage of shift of the curves, in every combination of tiles and integration times. The values appear to be significant, with peaks that focus mainly along a specific integration time (40 ms for VNIR and 12 ms for SWIR) and along the gray target, which is built in a different material with respect to the rest. We have to bear in mind that the optimization is run for all tiles simultaneously and the best compromise forcefully prioritizes the most represented material in the *unbalanced* sample set.

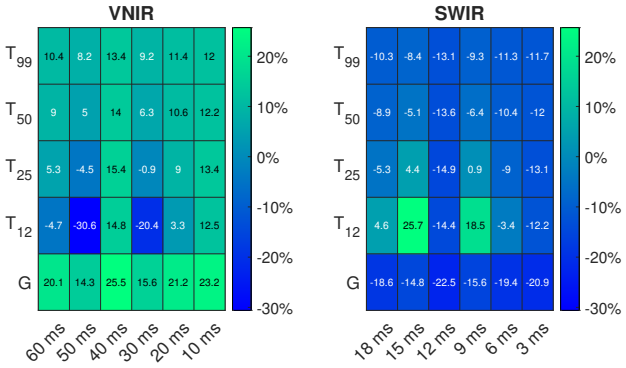

Figure 8. *Percentage of shift after correction. The values are significant with peaks concentrating along a specific integration time (40 ms for VNIR, and 12 ms for SWIR), and the gray tile, which is built with a different material than the rest.*

Discussion

The proposed optimization process allows to achieve reflectance curves that are more accurate than those obtained in the standard calibration procedure. Moreover, the radiance and reflectance curves are smoothly fused in the interval from 400 nm to 2500 nm, without presenting *jumps* in the shared spectral range. The correction can be seen as a function of the considered reflective tile and the integration time. However, such correction implies that the radiance equality property at different integration times is lost. There exists a trade-off between accurate spectral matching between cameras and uniformity of radiance within a single camera. In this work, we decided to prioritize the outcome of smooth and continuous reflectance curves, since most of the applications will involve reflectances, rather than radiance quantities. We also observed an alleged material-dependence, as the results obtained on the gray Spectralon target did not follow closely the general behavior of the other targets.

We finally point out that the optimization was performed and then tested on the same dataset. This decision is taken considering that only a few standardized targets defined in the VNIR and SWIR range exist.

Conclusion

In this work, we highlighted the shortcomings of a simultaneous dual acquisition setup of hyperspectral imagery, in terms of spectral matching between the response curves of the two cameras. We proposed a solution based on the optimization of correcting factors that allow the spectral matching, exploiting an overlap area in the electromagnetic spectrum from 950 nm to 1000 nm. The linearity of both cameras were preliminarily assessed in terms of RAW and radiance signal response, varying the average reflectance of the considered samples, and the integration time of the acquisitions. As a possible line of future work,

the information regarding the signal to noise ratio of the cameras can be exploited to obtain wavelength-dependent correcting factors, in conjunction with smoothing procedures in the spectrally overlapping region. Moreover, we are currently assuming a perfectly specular acquisition set-up, adopting two lights belonging to the same family and model. However, it might be possible that such light sources produce illumination fields with different intensities in the radiance space. This could be the major cause for spectral mismatching, and identifying it could lead to modification in the set-up, or carefully designed post-processing steps.

References

[1] Eberhard H Lehmann, Peter Vontobel, Eckhard Deschler-Erb, and Marie Soares. Non-invasive studies of objects from cultural heritage. *Nuclear Instruments and Methods in Physics Research Section A: Accelerators, Spectrometers, Detectors and Associated Equipment*, 542(1-3):68–75, 2005.

[2] Guolan Lu and Baowei Fei. Medical hyperspectral imaging: a review. *Journal of Biomedical Optics*, 19(1):010901, 2014.

[3] Aoife Gowen, Colm O'donnell, Patrick Cullen, and Steven Bell. Recent applications of chemical imaging to pharmaceutical process monitoring and quality control. *European Journal of Pharmaceutics and Biopharmaceutics*, 69(1):10–22, 2008.

[4] John K Delaney, Kathryn A Dooley, Annelies Van Loon, and Abbie Vandivere. Mapping the pigment distribution of vermeer's girl with a pearl earring. *Heritage Science*, 8(1):1–16, 2020.

[5] Jay Pearlman, Stephen Carman, Carol Segal, Peter Jarecke, Pamela Clancy, and William Browne. Overview of the Hyperion imaging spectrometer for the NASA EO-1 mission. In *IGARSS 2001. Scanning the Present and Resolving the Future. Proceedings. IEEE 2001 International Geoscience and Remote Sensing Symposium (Cat. No. 01CH37217)*, volume 7, pages 3036–3038. IEEE, 2001.

[6] Gary A Shaw and Hsiaohua K Burke. Spectral imaging for remote sensing. *Lincoln Laboratory Journal*, 14(1):3–28, 2003.

[7] Christian Rogass, Friederike M Koerting, Christian Mielke, Maximilian Brell, Nina K Boesche, Maria Bade, and Christian Hohmann. Translational imaging spectroscopy for proximal sensing. *Sensors*, 17(8):1857, 2017.

[8] CIE Divison 8 CIE 223:2017, ISBN: 978-3-902842-10-7. Multispectral image formats. `https://cie.co.at/publications/multispectral-image-formats`, 2017.

[9] Torbjørn Skauli. Specifying radiometric performance of hyperspectral and conventional cameras: a minimal set of independent characteristics. In *Algorithms, Technologies, and Applications for Multispectral and Hyperspectral Imagery XXVI*, volume 11392, page 113920B. International Society for Optics and Photonics, 2020.

[10] John K Delaney, Jason G Zeibel, Mathieu Thoury, Roy Littleton, Kathryn M Morales, Michael Palmer, and E René de la Rie. Visible and infrared reflectance imaging spectroscopy of paintings: pigment mapping and improved infrared reflectography. In *O3A: Optics for Arts, Architecture, and Archaeology II*, volume 7391, page 739103. International Society for Optics and Photonics, 2009.

[11] Honglyun Park, Jaewan Choi, Nyunghee Park, and Seokkeun Choi. Sharpening the VNIR and SWIR bands of Sentinel-2A imagery through modified selected and synthesized band schemes. *Remote Sensing*, 9(10):1080, 2017.

[12] Laetitia Loncan, Luis B De Almeida, José M Bioucas-Dias, Xavier Briottet, Jocelyn Chanussot, Nicolas Dobigeon, Sophie Fabre, Wenzhi Liao, Giorgio A Licciardi, Miguel Simoes, et al. Hyperspectral pansharpening: A review. *IEEE Geoscience and remote sensing magazine*, 3(3):27–46, 2015.

[13] Massimo Selva, Bruno Aiazzi, Francesco Butera, Leandro Chiarantini, and Stefano Baronti. Hyper-sharpening: A first approach on SIM-GA data. *IEEE Journal of selected topics in applied earth observations and remote sensing*, 8(6):3008–3024, 2015.

[14] Kwok-Keung Wong. Development of co-boresighted VIS-NIR-SWIR hyperspectral imaging systems. In *Spectral Imaging Sensor Technologies: Innovation Driving Advanced Application Capabilities*, volume 9104, page 910405. International Society for Optics and Photonics, 2014.

[15] Lucien Wald, Thierry Ranchin, and Marc Mangolini. Fusion of satellite images of different spatial resolutions: Assessing the quality of resulting images. *Photogrammetric engineering and remote sensing*, 63(6):691–699, 1997.

[16] Andreas Baumgartner, Peter Gege, Claas Köhler, Karim Lenhard, and Thomas Schwarzmaier. Characterisation methods for the hyperspectral sensor HySpex at DLR's calibration home base. In *Sensors, Systems, and Next-Generation Satellites XVI*, volume 8533, page 85331H. International Society for Optics and Photonics, 2012.

[17] Thomas Coleman, Mary Ann Branch, and Andrew Grace. Optimization toolbox. *For Use with MATLAB. User's Guide for MATLAB 5, Version 2, Relaese II*, 1999.

[18] Paul E Debevec and Jitendra Malik. Recovering high dynamic range radiance maps from photographs. In *ACM SIGGRAPH 2008 classes*, pages 1–10. 2008.

Author Biography

Federico Grillini *received his BSc degree in Optics and Optometry from the University of Florence (Italy) in 2017, and the MSc in Colour in Science and Industry from the joint Erasmus-Mundus program COSI (Universite Jean Monnet, Universidad de Granada, and NTNU) in 2020. Since the same year, he is a PhD candidate at the Norwegian Institute of Science and Technology (NTNU) in Gjøvik, Norway. His studies focus on hyperspectral imaging techniques for applications on cultural heritage.*

Jean-Baptiste Thomas *received his Bachelor in Applied Physics in 2004 and his Master in Optics, Image and Vision in 2006, both from Université Jean Monnet in France. He received his PhD from Université de Bourgogne in 2009. Since 2010, he is Associate Professor at the Université de Bourgogne. Between 2016 and 2019 he was in a research leave at NTNU. Since 2019 he is Associate Professor at NTNU. He has worked extensively on the development of spectral imaging systems through Spectral Filter Arrays technology. Since 2016 he has worked in understanding material appearance and its measure by using imaging systems. More information at http://jbthomas.org/.*

Sony George *is currently Associate Professor at The Norwegian Colour and Visual Computing Laboratory, Norwegian University of Science and Technology (NTNU) since 2017. Before joining NTNU, he has worked as a researcher at Gjøvik University College, Norway. Sony obtained a PhD in Photonics from the Cochin University of Science and Technology, India in 2012. His research interests are in the field of spectral imaging and its applications. He has been involved in several national and EU projects in different roles: EU MSCA-ITN projects: CHANGE, HiPerNav, COST action: COSCH, MultiForSee etc. email:sony.george@ntnu.no*